Composite Structures 311 (2023) 116811

Contents lists available at ScienceDirect

Composite Structures

journal homepage: www.elsevier.com/locate/compstruct

Effect of shear thickening gel on microstructure and impact resistance of ethylene–vinyl acetate foam

Huan Tu [a,1], Pengzhao Xu [b,c,1], Zhe Yang [d], Fan Tang [a,e], Cheng Dong [a,e], Yuchao Chen [a,e], Wenjian Cao [a], Chenguang Huang [a], Yacong Guo [a,*], Yanpeng Wei [a,*]

[a] Key Laboratory for Mechanics in Fluid Solid Coupling Systems, Institute of Mechanics, Chinese Academy of Sciences, Beijing, 100190, China
[b] School of Mechanical Engineering, Northwestern Polytechnical University, Xi'an 710072, China
[c] Xi'an Institute of Electromechanical Information Technology, Xi'an 710065, China
[d] Beijing CAS Mechanical Confidence Science and Technology Co., Ltd., Beijing, 100088, China
[e] School of Engineering Science, University of Chinese Academy of Sciences, Beijing, 100049, China

ARTICLE INFO

Keywords:
Composite foam
Shear stiffening gel
Impact resistance
Microstructural analysis

ABSTRACT

To satisfy the ever-increasing demand for better anti-impact performance of personal protective equipment, a composite foam by incorporating shear thickening gel (STG) with ethylene–vinyl acetate (EVA) was developed. The superiorities of EVA foam in softness, lightness and flexibility were maintained in the novel material. The microstructure of STG/EVA composite foam was characterized using Scanning Electron Microscope. A series of experimental approaches including Dynamic Mechanical Analysis test, compression test, Split Hopkinson Pressure Bar test and drop hammer test were applied to study the material properties at different strain rates. Attributed to the shear thickening property of STG, STG/EVA exhibited significant strain rate sensitivity. The results showed that STG/EVA foam possessed better mechanical performance than plain EVA foam. In the ballistic test, the body armor consisting of the STG/EVA buffer layer possessed better protective performance than the regular one. The improvement mechanism was interpreted with micromorphological changes before and after tests. The introduced STG reinforced the integrity and continuity of microstructure to enhance the capability of the composite material in absorbing and dissipating impact energy. Therefore, the application prospect of the developed STG/EVA foam in personal protective equipment is promising.

1. Introduction

Shear thickening gel (STG) is one kind of shear thickening material (STM), which has attracted the great attention of researchers in recent decades. In comparison with other types of polymer materials, the uniqueness of STG is manifested in the pronounced increment of modulus or viscosity with the increasing strain rates, which is called the shear thickening property [1–8]. Under normal circumstances, STG exhibits viscoplastic properties with low modulus and behaves like plasticine [9]. However, impact loads will stimulate the phase transition of STG among plastic, rubbery and solid states and the stiffness of material will raise instantly [10–12]. With in-depth study of STM, the intelligent property of self-adaptive stiffness over the intensity of external force has been gradually deliberated by researchers. Since STG is a kind of boron-siloxane polymer silicon rubber, a large number of dynamic boron-oxygen (B-O) weak cross-links exist, in which the formation and breakage are dynamically reversible. Under natural condition, the rate of B-O cross-links breakage is greater than the rate of STG deformation. Thus, these unstable chemical bonds lead to the viscous behavior of the material. The phase change of STG from gel state to glassy state will be produced by high strain rate effects, for instance, oscillations and impacts. Due to the lower rate of B-O cross-links breakage than loading rate, molecular chains bridged by the B-O bonds will entangle between each other to enhance the intermolecular force. Hence, the instantaneous hardening reaction of STG is ascribed to the "Jamming effect" of molecular chains inside [13,14].

Unstable intermolecular structures result in a typical cold-flow behavior of STG, viz., a slow deformation under gravity [15]. Though STG owns huge potential and broad prospect in many domains, the cold-flow problem heavily constrains the direct application. Researchers are

* Corresponding authors.
E-mail addresses: guoyacong@imech.ac.cn (Y. Guo), weiyanpeng@imech.ac.cn (Y. Wei).
[1] Contributed equally in this work.

https://doi.org/10.1016/j.compstruct.2023.116811
Received 13 September 2022; Received in revised form 26 December 2022; Accepted 11 February 2023
Available online 22 February 2023

working to find out practicable approaches to utilize the anti-impact superiority of STG. Tang et al. [14] encapsulated STG into a Teflon mold as a buffer pad of a body armor. The protective capacity of the novel body armor was much greater than that of the conventional one. However, in comparison with commonly used buffer materials, the STG pad is much heavier and the long-term stability of STG pads depends on the quality of encapsulation. Using STG as the core material in sandwich structures is the other applicable technique put forward by researchers [16,17]. The shape change of STG over time will be inevitable if no effective constraint is provided. To overcome flowability-induced drawbacks, researchers attempted to use STM as the reinforcement of fiber fabrics to enhance energy absorption capacity [18–20]. Impregnating shear thickening fluid (STF) into fabrics is a feasible method to improve impact toughness without flexibility loss [21–25]. To satisfy the increasing requirement for protection, STG has been introduced into ballistic fabrics in recent studies. He et al. [26] developed novel composite laminates by doping STG into STF-impregnated-Kevlar woven fabric. The test results showed that both the bullet-proof performance and stability of the fabric were improved with the assistance of STG. In addition, ascribed to its rate-dependent phase change properties, STM was widely applied in various areas, such as cutting tools [27], vibration damping systems [28], electronic devices [29] and shock absorbers [30].

The successful combination of STG with fabrics through physical means evokes the research interest in producing STG-modified polymer materials. The progress of synthetic technology promotes the creation of new compounds. To improve the performance of conventional polymers under extreme loading conditions, a hot spot of recent research is the development of STG reinforced composites. Liu et al. [31] conducted a systematic study on shear thickening gel/polyurethane foam (STG/PU) to explore the relationship between the molecular structure and material properties. Microscopic test methods were used to detect the change of chemical bonds and molecular chains due to the incorporation of STG. Two key findings were reported in the work: 1) no new chemical bond between STG and PU was formed during the blending process; 2) the intertwined molecular chains between STG and PU lead to higher thermal stability. Moreover, the novel composite possessed better mechanical properties than the plain PU foam, which demonstrated the potential of using STG synthesized materials in human protective equipment. Fan et al [32] put forward new fabrication methods by dip-coating or spray-coating STG on PU foam. To satisfy multiply functional requirements such as electrical conductivity, hydrophobicity and energy absorption capability, carbon nanotubes or nano-SiO_2 were blended with STG as the coating. The test results showed that the multifunctional composite foam possessed outstanding safeguarding, sensing and superhydrophobic performance that the regular foam materials lack.

The development of personal protective equipment has lasted for several centuries. As the research moves along, it is found that a wearer would suffer injury even though bullets have been prevented by a body armor, which is called “behind-armor blunt trauma” (BABT) [33]. Nowadays, to provide better protection and to reduce BABT, a buffer layer commonly made of ethylene–vinyl acetate (EVA) foam is placed behind ballistic layers. The effectiveness of mouthguards made of EVA in preventing tooth or maxillofacial trauma has been proven by A. Messias et al [34]. Attributed to the great flexibility, elasticity and stability, EVA buffer layer could absorb a part of impact energy and relief the contact force between the armor and the human body. However, regular EVA foam owns limited energy absorption capacity. In this study, a new type of composite foam was developed by introducing STG into EVA. The STG/EVA foam possessed characteristics of softness, resilience, and outstanding impact resistance. The mechanical properties under different strain rates were determined by corresponding test approaches. In addition, the microstructure and surface morphology of the composite were observed through the electron microscopic technique. The damage mode in the microscopic scale discovered the failure mechanism of the synthetic material and the improvement effect of the additive STG. The excellent anti-impact performance showed the huge potential and the bright prospect of the STG reinforced EVA foam in personal protective equipment.

2. Materials and methods

2.1. Materials

The raw materials included boric acid, hydroxyl-terminated polydimethylsiloxane (PDMS-OH), EVA, calcium carbonate ($CaCO_3$), AC foaming agent, zinc oxide (ZnO), stearic acid and dicumyl peroxide. All the chemicals were supplied by CAS Mechanical Confidence Science and Technology Co., ltd. (Beijing, China). No further purification and reprocessing were needed before preparation.

2.2. Preparation of STG/EVA composite foam

Preparation of STG: the whole process was elaborated in a published paper [14]. Boric acid and PDMS-OH at a mass ratio of 1:5 were mixed uniformly and then stirred in an oven at 160–180 °C for 2–3 h. The blend was cooled down to form synthesize polyborosiloxane, viz., STG.

Preparation of STG/EVA foam: at the first step, mixed STG with other chemicals (the mass ratio of STG, EVA, CaCO3, ZnO, stearic acid and dicumyl peroxide = 55: 3.5: 10: 2.4: 1: 0.5: 0.54) in a heated mixer at 100–120 °C for 10 min. Then, moved the thoroughly stirred mixture into a milling machine for refinement. The distance between two rollers and the velocity of rotation were adjusted during the operation to guarantee the machining quality. Lastly, all the reactants were poured into a mold and placed in a vulcanizing machine for the foaming process. Appropriate temperature and pressure of vessel were pre-set. The mixture expanded during the reaction process and the final volume was controlled by the sealed mold. The whole process of preparation is shown in Fig. 1. In this study, the density of the produced STG/EVA foam was about 0.68 g/cm^3.

2.3. Material characterization

The macroscopic and microscopic morphology of the composite foam were characterized. As shown in Fig. 2, the prepared STG was gel-like material and exhibited typic cold-flow behavior, viz., obvious shape change under gravity. Fig. 3 (a) and (b) are the photography of EVA and STG/EVA foam. Since only a small amount of STG was added, the density of STG/EVA (0.68 g/cm^3) was close to that of EVA (0.65 g/cm^3). Intuitively, the appearance of the regular and modified materials was quite similar, which were solid, white and porous. To observe the microscopic morphology and explore the influence of STG on EVA microstructure, a scanning electron microscope (SEM, Hitachi S4800) was used for both EVA and STG/EVA samples. Fig. 3(c) is the SEM image of EVA foam, which shows a large number of uneven voids were formed inside. In the magnified SEM photography [Fig. 3(d)], it was found that EVA foam owned a thin-walled microstructure. The inner space was divided by the matrix material and the cellular units were not interconnected. The SEM image of STG/EVA [Fig. 3(e)] shows the size of voids tended to be more uniform and clusters of tiny voids were almost eliminated compared with the regular EVA. As observed in Fig. 3(f), STG covered the EVA skeleton like a coated film and filled parts of the voids. Thus, the interconnection between cellular units was established through the STG film. In addition, STG particles were distributed and attached to the EVA skeleton to roughen the surface. Fig. 4 is a 3D schematic diagram of STG/EVA composite foam and plain EVA foam to clearly present their micromorphology. Based on the differences in microstructural characteristics between EVA and STG/EVA, the composite foam might possess better toughness due to the uniformity of voids. Stress concentration more likely occurred in the region of uneven layout to result in localized failure. Consisting of cellular units of an approaching size, the consistency of deformation in STG/EVA foam was

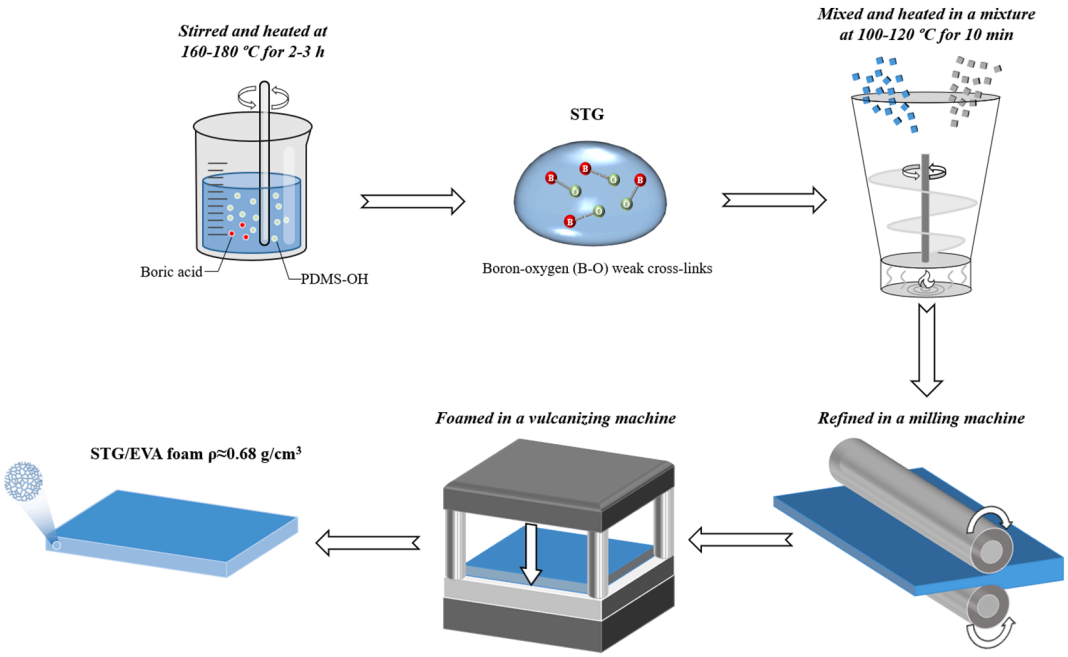

Fig. 1. Preparation process of STG/EVA foam.

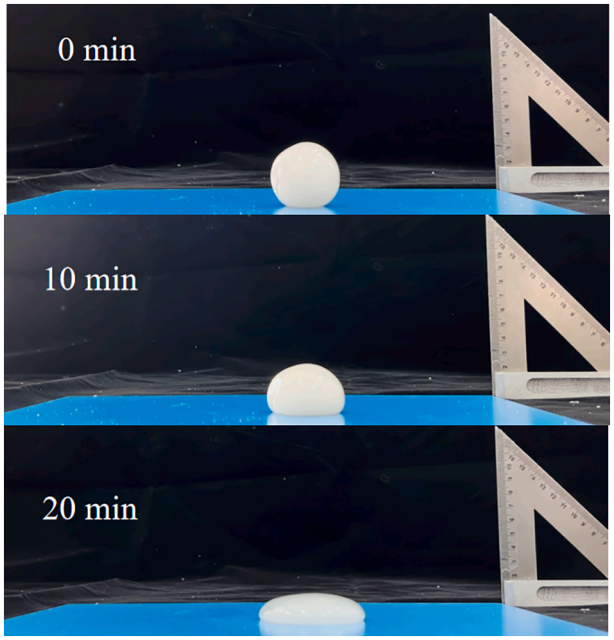

Fig. 2. Cold-flow behavior of STG.

better, which was manifested as the improvement of toughness in mechanical property. This characteristic was further reinforced by the interconnection of STG. Moreover, stretching and tearing of STG particles contributed to dissipating and absorbing energy during the loading process, which was another mechanism to toughen the composite foam.

2.4. Dynamic mechanical analysis test

Dynamic Mechanical Analysis (DMA) is a widely used technique to determine the elastic and viscous response of polymer composite under oscillating loads as well as to characterize the amorphous phase transitions of polymers [35]. To obtain the thermal transition parameters such as glass transition temperature T_g and rubbery transition temperature T_r is the primary objective of the DMA test [36–38]. In recent studies, researchers are working to expand the utility of the DMA technique to investigate the dynamic properties of materials [39,40]. Besides, bridging the relationship between mechanical behavior and microstructure through the DMA measurements is a potential application [41,42].

DMA tests were conducted by a TA instrument (USA) Q800 DMA. Cylindrical specimens in the dimension of 15 mm (diameter) × 7.5 mm (height) were prepared. Compression test mode with uniaxial oscillation loading was employed. Normally, DMA testing consists of two phases, temperature sweep mode and frequency sweep mode. Since the emphasis of this study was to investigate the material behavior under dynamic loading, the temperature was fixed at 25 °C (room temperature) and the loading frequency varied from 0.01 to 150 Hz.

2.5. Compression test

Ascribed to the shear thickening property of STG, the composite foam possessed significant strain rate sensitivity. It was imperative to obtain the basic mechanical property of STG/EVA under compression. Compression tests were conducted using a universal test system and the geometry of cylindrical specimens was 15 mm (diameter) × 5 mm (height). The strain values were automatically measured by the extensometer equipped on the test system. Three strain rate levels (0.001, 0.01 and 0.1 s^{-1}) were achieved by adjusting loading speed. Three tests were repeated at each strain rate to obtain reliable and valid results.

2.6. Split Hopkinson pressure bar test

Due to the limited capacity of the universal testing machine, the dynamic compressive property of composite foam at higher strain rates was obtained by using the Split Hopkinson Pressure Bar (SHPB) system. The SHPB system mainly consists of a strike bar, an incident bar, a transmission bar and a data collection system, as illustrated in Fig. 5. The strike bar was driven by pressured gas to impact the incident bar. The striking velocity was adjustable by controlling the gas pressure to achieve different strain rate effects. The generated stress wave propagated through the incident bar and reached the surface of the specimen. The difference in material property between the bar and the specimen

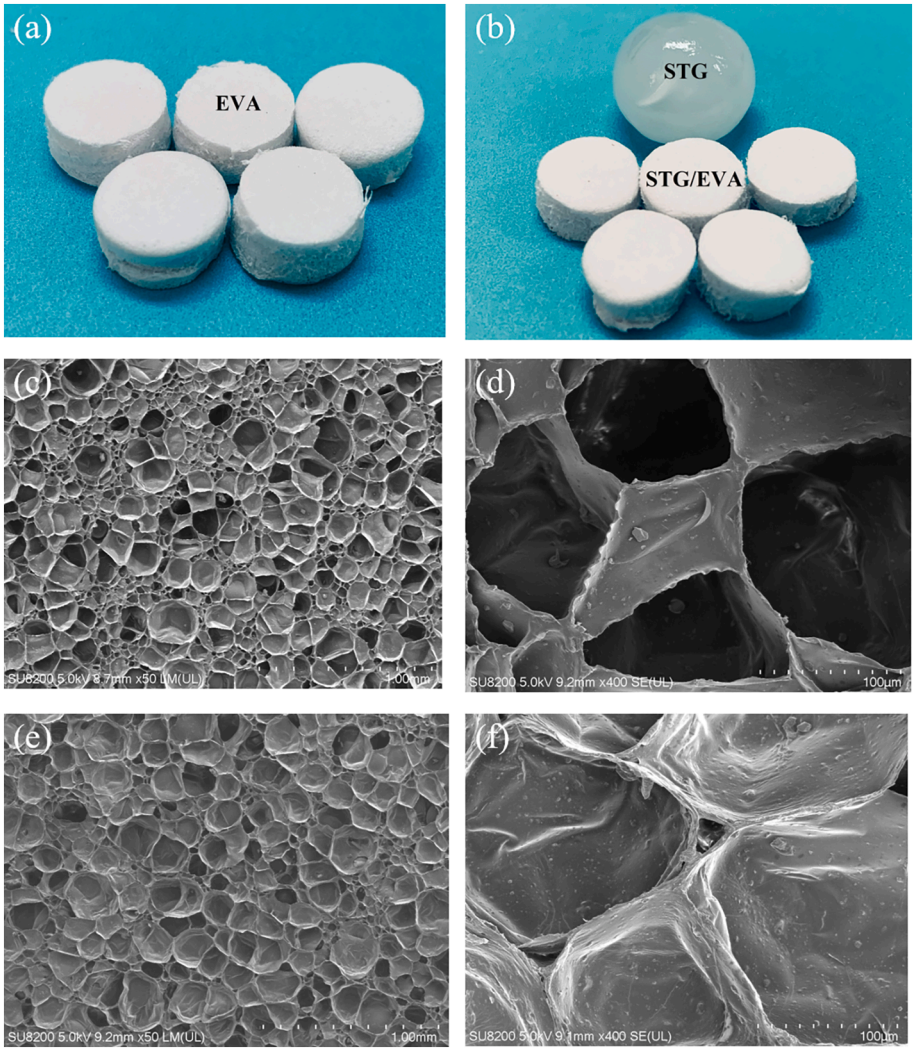

Fig. 3. Macroscopic image of (a) EVA and (b) STG/EVA; (c) and (d): SEM images of EVA; (e) and (f): SEM images of STG/EVA.

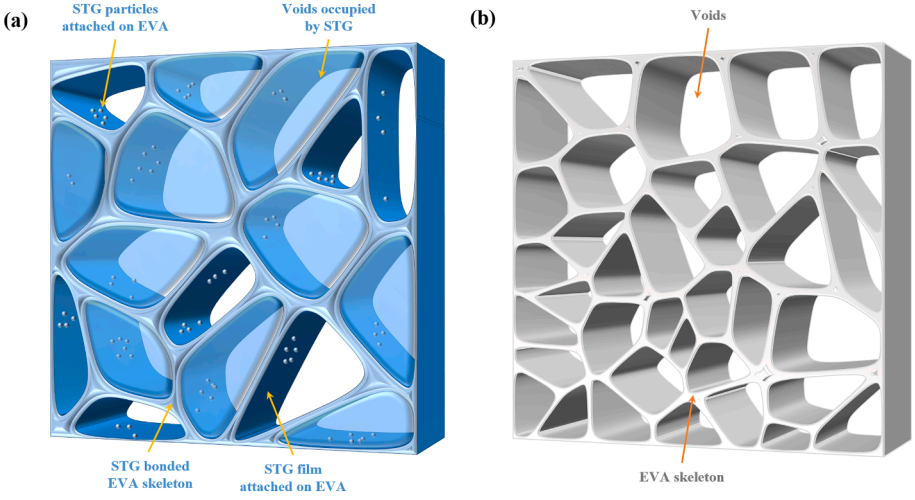

Fig. 4. 3D schematic diagram of micromorphology of (a) STG/EVA; (b) EVA.

resulted in the reflection and transmission of the stress wave at the interface. The transmitted wave continued to pass through the specimen and propagate to the transmission bar. Strain gauges were attached to the incident bar and the transmission bar to capture the strain signals and the stress values were calculable using Hooke's law. Based on the assumption that the specimen was in a stress equilibrium state, the stress ($\sigma(t)$), strain ($\varepsilon(t)$), and strain rate ($\dot{\varepsilon}(t)$) could be calculated by Eq. (1) - (3) with the measured incident wave ($\varepsilon_i(t)$), reflected wave ($\varepsilon_r(t)$), and

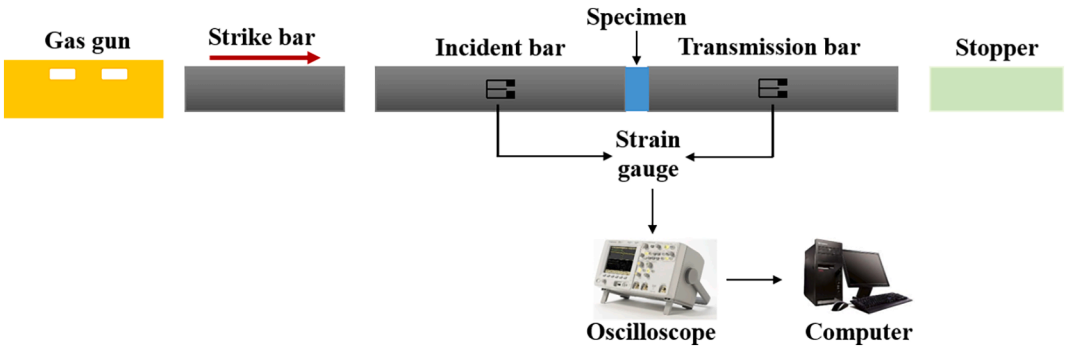

Fig. 5. Schematic of the SHPB test system.

transmitted wave ($\varepsilon_t(t)$) [43,44].

$$\sigma(t) = \frac{EA_0}{2A_s}[\varepsilon_i(t) + \varepsilon_r(t) + \varepsilon_t(t)] \quad (1)$$

$$\varepsilon(t) = \frac{C_0}{l_s}\int_0^t [\varepsilon_i(t) - \varepsilon_r(t) - \varepsilon_t(t)]dt \quad (2)$$

$$\dot{\varepsilon}(t) = \frac{C_0}{l_s}[\varepsilon_i(t) - \varepsilon_r(t) - \varepsilon_t(t)] \quad (3)$$

Where E, A_0 and C_0 are elastic modulus, cross-section area, and longitudinal wave velocity of the bars, respectively. A_s and l_s are the cross-section area and length of tested samples, respectively.

Due to the softness of foam materials, aluminium alloy bars were used instead of stainless-steel ones to reduce the mismatching impedance influence. Besides, semiconductor gauges were used due to the advantage of high sensitivity and resolution. The specimens were prepared in a cylindrical shape with a geometry of 15 mm (diameter) × 5 mm (height). The diameter of specimens was slightly smaller than that of bars (19 mm), which was helpful to eliminate the influence of friction in the lateral direction. Before each test, a plastic pulse shaper was placed at the end of the incident bar to smoothen the waveforms and reduce noise [45–47].

2.7. Drop hammer test

Drop weight test is a straightforward method to simulate the impact loading. The lifted block is accelerated by gravity to a prescribed velocity and then strikes the target. Fig. 6 is the schematic diagram of the drop hammer test system. In the experiment, a 5 kg weight was freely dropped from a 0.5 m height onto the center of specimens. The rounded impactor with a diameter of 50 mm was made of steel. To eliminate the influence of boundary, 500 × 500 mm foam plates with a thickness of 5 mm were prepared as specimens. A high-speed camera was prepared to shoot the whole impact process. In addition, Tekscan® distributed pressure sensor (USA) was placed at the rear face of specimens to capture pressure signal. The sampling frequency and the measurement range of the sensor were 20000 Hz and 0.0045 ~ 20.685 MPa, respectively. Based on the recorded resultant force and pressure, the buffering capacity of foam materials could be quantified to assess the impact resistance.

2.8. Ballistic impact test

As reviewed hereinbefore, a soft body armor commonly consists of ballistic layers and buffer layers. 42 layers of ultra-high molecular weight polyethylene (UHMWPE) laminates with the layer thickness of 0.15 mm were used as the ballistic layers of the tested body armor. The buffer layer was made of EVA or STG/EVA foam and the layer thickness

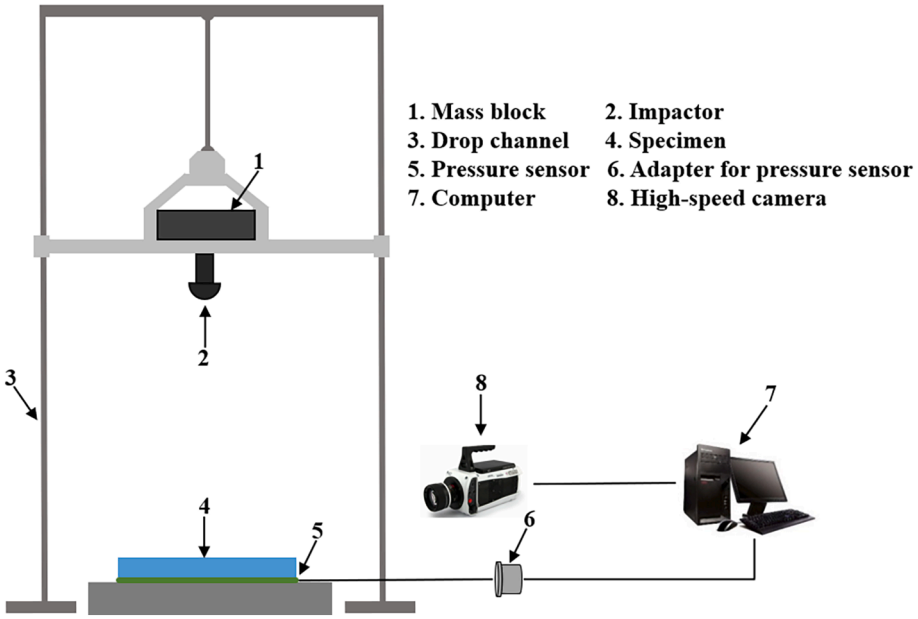

Fig. 6. Schematic of the drop hammer test system.

was 5 mm. All ballistic tests were completed in an authoritative testing institution to guarantee the reliability of the experimental platform. The set-up of the ballistic impact test is shown in Fig. 7, which followed the Chinese GA-2 protection standard (equivalent to US NIJ- IIIA) for body armor testing. Type 51 bullet (7.62 mm in diameter, 5.60 g in mass) was used and the prescribed velocity was 445 ± 10 m/s. The ballistic clay behind the body armor was the alternative to the human body and the depth of the crater (the backface signature) formed on the clay was a key indicator to evaluate BABT. Tekscan® distributed pressure sensor was placed on the rear face of the buffer layer to measure the contact pressure near the impact region. Moreover, the whole process of bullet impact was shot by the high-speed camera.

3. Results and discussion

3.1. DMA test

Storage modulus (E') and loss modulus (E'') are two major parameters obtained from DMA tests, which are the measure of the ability to store energy elastically and dissipate energy due to viscous response, respectively [48,49]. As the indicator of elasticity and viscosity of material, the characteristics of material under different strain rates could be interpreted with E' and E''. Clearly shown in Fig. 8, both E' and E'' of STG/EVA were greater than those of EVA. With the increasement of compression frequency from 0.01 Hz to 150 Hz, E' of STG/EVA varied from 0.327 MPa to 1.415 MPa, while the change of E' of EVA was from 0.153 MPa to 0.756 MPa. The difference in storage modulus between the modified and the plain foam material tended to be more distinct at higher loading frequency, which indicated that STG/EVA possessed significant strain rate sensitivity. A similar tendency could be observed in the test results of loss modulus. When the frequency was changed from 0.01 Hz to 150 Hz, E'' of STG/EVA and EVA increased from 0.066 MPa and 0.032 MPa to 0.356 MPa and 0.203 MPa, respectively. In general, the loss modulus of STG/EVA was 95 % higher than that of EVA. Based on above results, it was concluded that the elasticity and viscosity of EVA foam could be improved simultaneously by the incorporated STG material. In addition, the superiorities of STG/EVA in resisting and dissipating external excitation became more pronounced with increasing loading rate, which was ascribed to the shear thickening property of STG.

3.2. Compression test

It was imperative to determine the basic mechanical properties of materials before in-depth studies. As mentioned hereinbefore, the potential application of the developed foam material is in personal protective equipment. Thus, compressive performance is the most concerning material property. Fig. 9(a) displays the stress–strain curves of STG/EVA and EVA under different speeds of compression and the equivalent strain rate ($\dot{\varepsilon}$) of the respective test group is 0.001, 0.01 and 0.1 s^{-1}. STG/EVA and EVA behaved like typical foam materials, whose initial young's modulus was minimal but the stiffness increased rapidly under high compression. As shown in Fig. 9(a), the stress–strain relationship of STG/EVA and EVA was almost identical at a strain rate of 0.001 s^{-1}. When the loading process was speeded up, the difference in compressive capacity between the composite and plain EVA became more and more prominent. At the highest strain rate ($\dot{\varepsilon}$=0.1 s^{-1}), the peak stress of STG/EVA nearly doubled to that of plain EVA. Since STG owned apparent strain rate sensitivity, the material properties of the composite foam were heavily affected by the loading rate. It was worth noting that the stiffness of STG/EVA was improved significantly under highly compressed conditions while the increasement was not pronounced at the beginning of loading. This phenomenon could be interpreted with the SEM observations shown in Fig. 3. The inner space of EVA foam was occupied by the matrix material and plenty of voids. When the external force was applied, voids were compressed firstly which led to ease of deformation. With the elimination of voids, the matrix material gradually played a dominant role in bearing the loading. As discussed in Section 2.3, STG was bonded with EVA matrix in the form of coated films and dispersed particles. Thus, at the initial stage

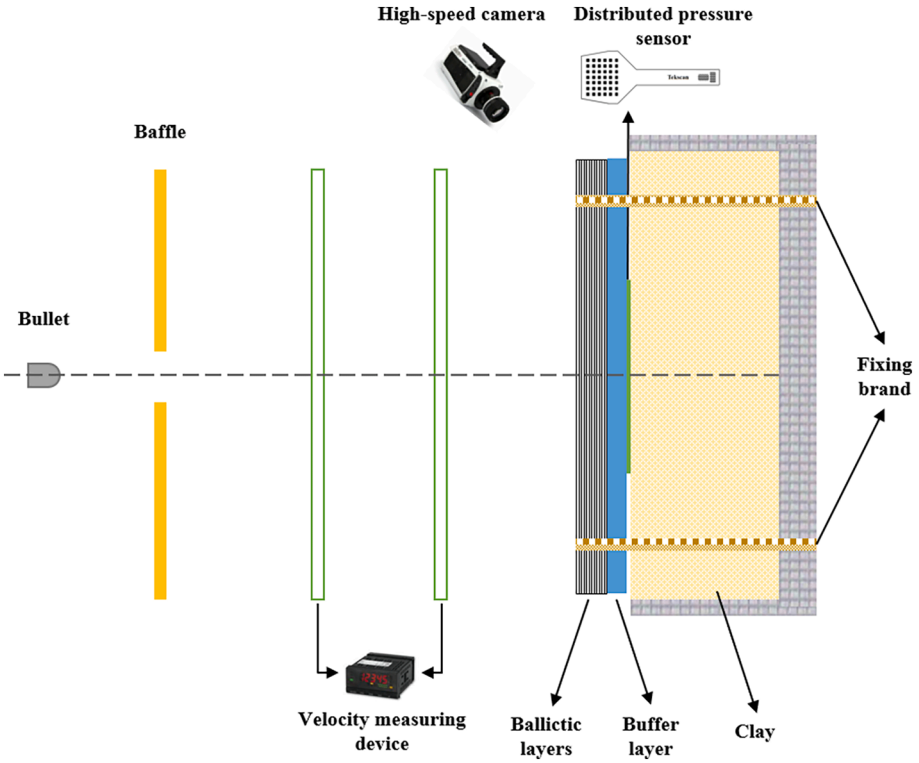

Fig. 7. Schematic of the ballistic impact test system.

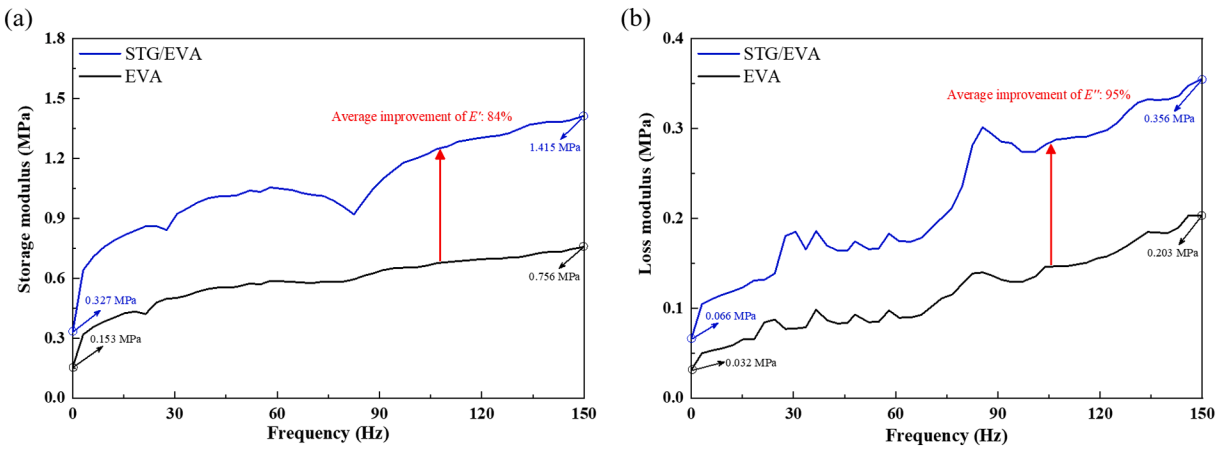

Fig. 8. DMA test results of EVA and STG/EVA: (a) storage modulus; (b) loss modulus.

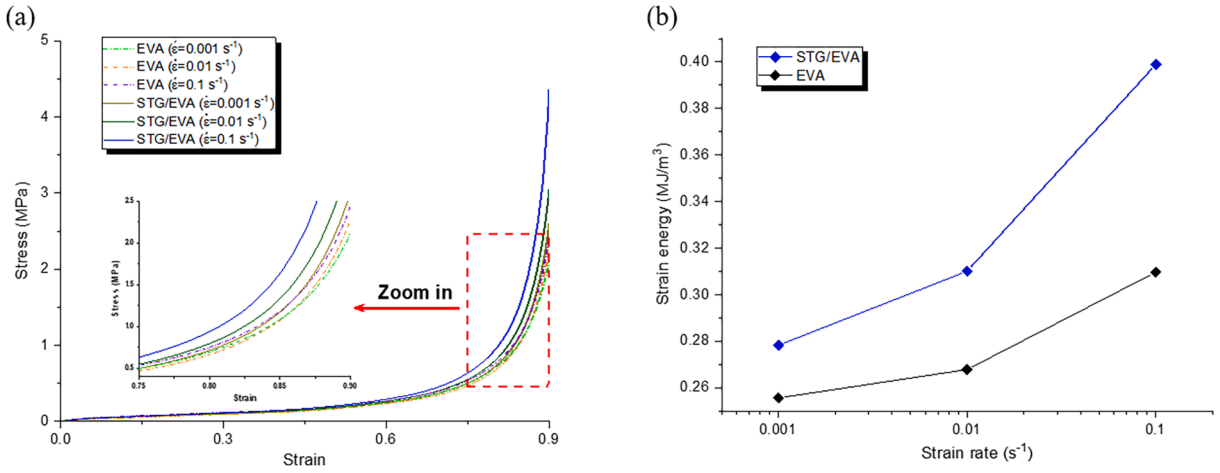

Fig. 9. (a) Stress–strain curves of EVA and STG/EVA at 0.001, 0.01 and 0.1 s^{-1} strain rates; (b) strain energy of EVA and STG/EVA at 0.001, 0.01 and 0.1 s^{-1} strain rates.

that was dominated by the voids, the influence of STG on mechanical behavior is limited. STG would assist the matrix material to resist deformation when most voids closed up. The strain energy represented the energy absorption capacity of material during compression. By calculating the area enclosed by the stress–strain curve and x-axis, the strain energy of each test group is obtained and plotted in Fig. 9(b). It clearly showed that STG could endow EVA foam with greater strain energy and higher strain rate sensitivity, which were practical in anti-impact protective equipment.

3.3. SHPB test

Due to the limited capacity of the universal testing machine, the SHPB system was used to achieve higher strain rate effects. The stress–strain curve of each specimen was calculated by Eqs. (1) and (2) and the corresponding strain rate was estimated using Eq. (3). The strain rate of specimens during compression was controlled by adjusting the launching pressure and two strain rate levels ($\dot{\varepsilon}$=260 and 1900 s^{-1}) were implemented in the present study. The stress–strain relationship at a relatively low strain rate (dash lines in Fig. 10) could be approximated as linear and the slope represented the elastic modulus of the foam materials. As the deformation at the initial stage was induced by compaction of voids, the contribution of STG to resist external loading was minor and the compressive capacity of STG/EVA and EVA was close. However, the differences became prominent at a strain rate of 1900 s^{-1}, which were solid lines in Fig. 10. Based on the microstructure images of STG/

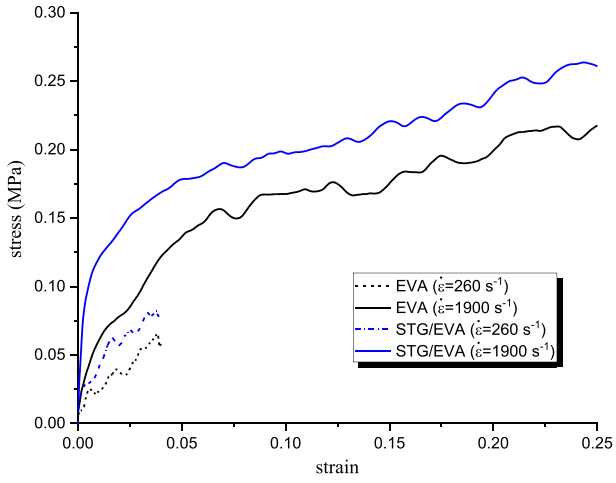

Fig. 10. SHPB test results of EVA and STG/EVA at 260 and 1900 s^{-1} strain rates.

EVA foam, it was found that part of the voids was occupied by STG material. Hence, the behavior of voids during compression was affected by STG filler to a certain extent. It was rational to infer that the enhancement of elastic modulus and compressive strength at a high

strain rate was mainly attributed to the shear thickening property of STG.

3.4. Drop hammer test

The buffering capacity of foam materials to the human body was tested by a drop hammer system. Though the hammer did not penetrate the specimens, the impact energy would propagate to the rear face in the form of stress waves and lead to depressed deformation. Excessive contact pressure between the protective equipment and the human body would cause severe injury. Therefore, a distributed pressure sensor was used to record the essential mechanical parameters. As shown in Fig. 11, the distribution of pressure on EVA and STG/EVA specimens was concentrated, where the magnitude of stress attenuated rapidly from the impact point to the surrounding region. In comparison with plain EVA, the peak pressure at the rear face of the STG/EVA specimen was 30 % lower, which represented the better anti-impact performance of the composite foam. This prominent enhancement was ascribed to higher elasticity and viscosity of STG/EVA. DMA test results showed that the storage modulus and loss modulus of EVA foam were improved simultaneously by introducing STG. Hence, the impact energy could be more effectively dissipated in the composite material through viscous behavior. Moreover, STG increased the resilience and stiffness of EVA matrix and restrained the relative deformation. The significant relief of rear pressure proved that STG/EVA foam could provide considerable protection for the human body under impact loading.

3.5. Ballistic impact test

The real weapon effect could be reproduced by the ballistic impact platform. The set-up followed the standard and was elaborated in Section 2. 7. The whole process of bullet impact shown in Fig. 12 was shot by the high-speed camera. As a type of fabric, the out-plane strength of UHMWPE was relatively low and the laminates failed in tension and shear modes under lateral impact. Due to the fracture of fabrics, certain bulletproof layers were penetrated by the bullet. The damaged layers on each body armor were counted and the number in all tests was identical, which indicated the consistency of tested specimens and impact loading. Except for penetrating multiplayer UHMWPE, the striking bullet would drive the remaining laminates to deform and squeeze the buffer layer. As the most important index to evaluate the protective capacity of body armor, the depth of the crater (the backface signature) was measured using a caliper as shown in Fig. 13(a). The measurement of crater depth followed the Chinese GA-2 protection standard as sketched in Fig. 13(b). A distributed pressure sensor was placed on the rear face of the buffer layer to capture the pressure value. The test results were summarized in Table 1. It was worth noting that the crater depth on ballistic clay was reduced by 51 %, from 11.4 mm to 5.6 mm, when the plain EVA was replaced by the STG/EVA composite foam. The significant enhancement in deformation resistance indicated that the possibility of severe injury to vital organs could be drastically reduced. Besides, the peak force and peak pressure on the surface of clay were lowered moderately due to the protection of the composite buffer layer. The peak value of contact force and contact pressure could not fully reflect the anti-impact performance of materials. Fig. 14 showed the pressure distribution around the impact region. As displayed in Fig. 14(a), two stress concentration areas were produced, which indicated that the response of the EVA buffer layer was localized and discontinuous. On the contrast, multiple pressure peaks in Fig. 14(b) demonstrated that a larger area of STG/EVA material participated in resisting impact loading.

To better understand the mechanisms to cause the difference in anti-impact performance, the microstructure of post-test foam materials was observed using SEM. As illustrated in Fig. 15(a) and (b), which were SEM images of post-impact EVA and STG/EVA samples respectively, two distinct areas called impact region and peripheral region were formed due to stress wave generation, propagation and attenuation. Fig. 15(c) and (e) clearly demonstrated that the EVA material in the impact region was highly deformed and distorted while the most of peripheral foam almost remained intact and the change in morphological characteristic was not significant compared with undamaged specimens. In addition, a small number of cellular units suffered to moderate damage [Fig. 15(f)]. The distinct boundary between the impact region and the peripherical region reflected that the impact energy hardly transmitted outwards and the deformation was concentrated. In the magnified photo Fig. 15(d), the behavior of each cellular unit seemed to be independent without interconnection. The failure mode was in buckling and the thin-walled EVA skeleton lost its strength and stability due to plenty of crinkles formed. In comparison plain EVA, STG/EVA exhibited apparently different micromechanical behavior. Firstly, the extent of damage in the impact region was considerably severe where the skeleton structure was heavily crushed and the internal cellular units were hardly distinguished. In the SEM photo with higher magnification [Fig. 15(h)], it was found that the surfaces of post-impact material became rough and the STG/EVA composite was fractured into filaments. The observed damage pattern reflected that a large amount of impact energy was consumed by the breakage of matrix material and the entanglement of formed filaments. Secondly, STG/EVA in the peripherical region also suffered to serious damage as shown in Fig. 15(i). The material was considerably compressed while the contour of the thin-walled structure was still clear. Due to the existence of STG, the interconnection of adjacent cellular units was established. The stress wave could effectively propagate outward and more composite foam was involved to dissipate the impact

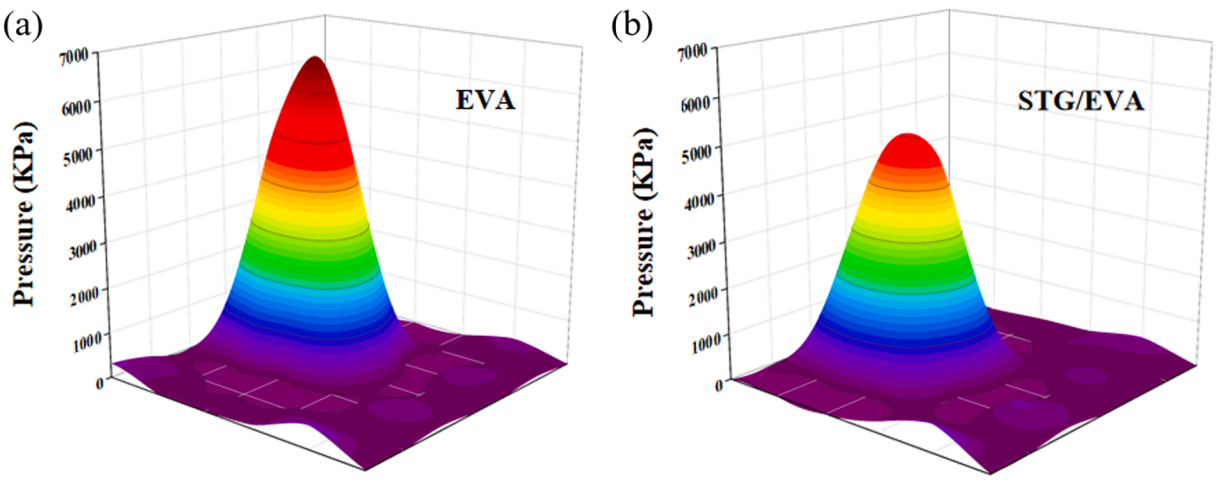

Fig. 11. Pressure distribution at the rear face of (a) EVA specimen; (b) STG/EVA specimen.

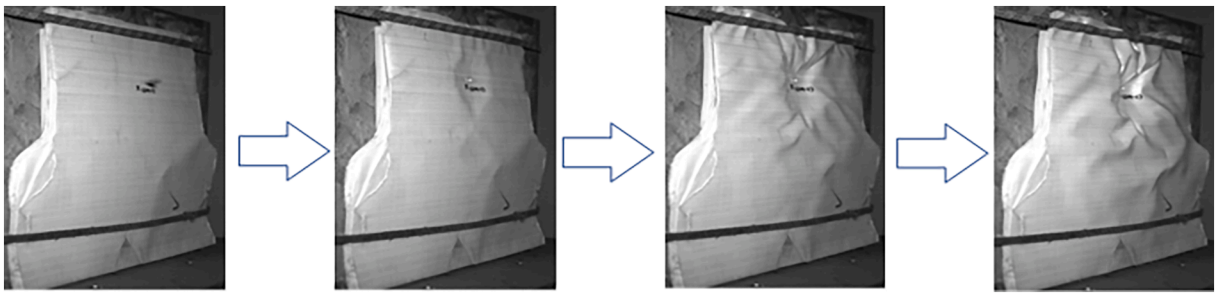

Fig. 12. Bullet impact process shot by the high-speed camera.

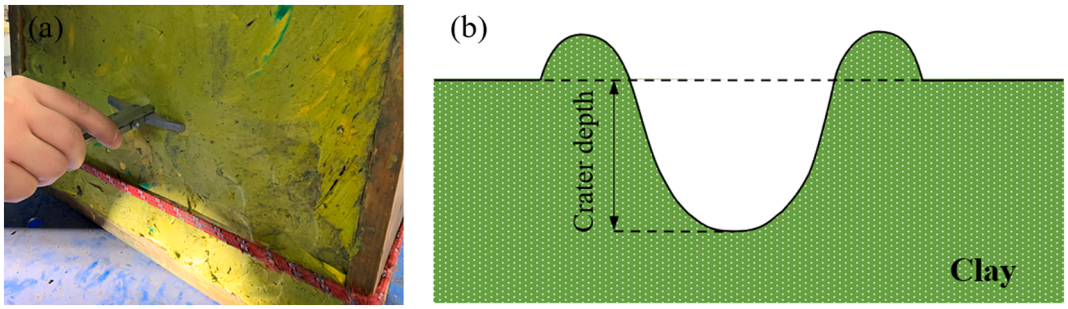

Fig. 13. (a) Photo of measuring the backface signature after ballistic tests; (b) definition of the backface signature.

Table 1
Ballistic test results of body armors with EVA and STG/EVA buffer pads.

Specimen	Impact velocity (m/s)	Crater depth (mm)	Peak force (KN)	Peak pressure (MPa)
UHMWPE+ EVA	450.3	11.4	0.400	1.57
UHMWPE+ STG/EVA	451.4	5.6	0.384	1.51

energy. Thirdly, STG itself participated in loading bearing. Attributed to its shear thickening property, STG was conducive to the improvement of microstructural integrity, especially under high strain rate conditions. Based on above analysis, the excellent anti-impact performance of STG/EVA owed to two major factors, which were outstanding energy absorption capacity of deformation and good continuity of microstructure.

4. Conclusion

In this study, a composite foam material by incorporating STG with EVA was developed to achieve outstanding personal protective capacity. The mechanical performance of STG/EVA at different strain rates was tested using corresponding experimental methods. In comparison with plain EVA foam, both elasticity and viscosity of the modified material were improved due to the introduced STG. The basic mechanical properties including compressive strength and strain energy of STG/EVA were enhanced with increasing strain rates. As the composite foam was intentionally used in body armors, the buffering capacity that was evaluated by the amplitude of rear pressure was a key indicator to assess the protection for the human body. Based on the results of drop hammer tests, STG/EVA possessed higher effectiveness in attenuating stress waves compared with EVA. Moreover, ballistic tests were conducted to investigate the anti-impact performance of the STG/EVA buffer layer against the actual weapon effect. The pronounced reduction in crater depth on ballistic clay demonstrated that the composite foam could improve the protective performance of body armors and lower the risk of blunt injury to vital organs. By using the microscopic instrument, the microstructure of STG/EVA before and after ballistic impact was observed to explore the essential material characteristics. The features of STG/EVA in morphology and damage mode demonstrated that the

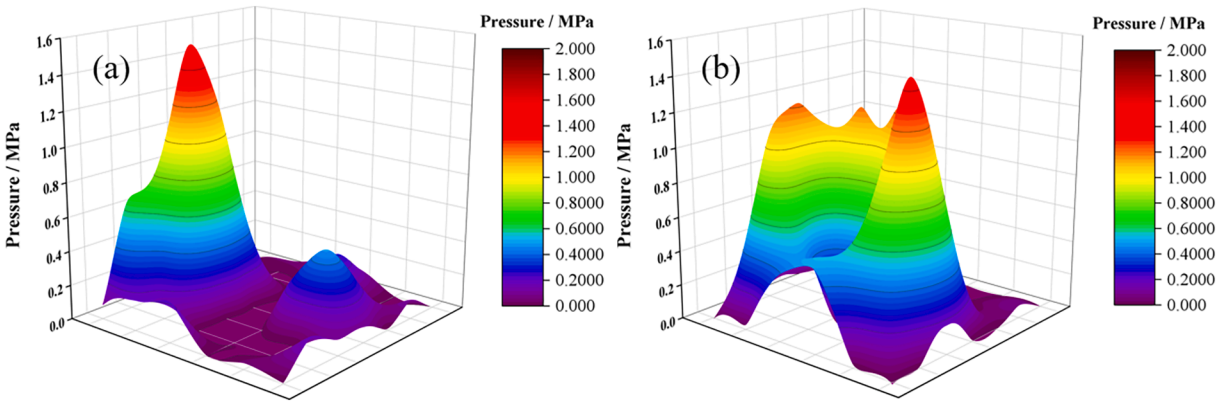

Fig. 14. Pressure distribution on the rear face of (a) UHMWPE + EVA and (b) UHMWPE + STG/EVA body armors.

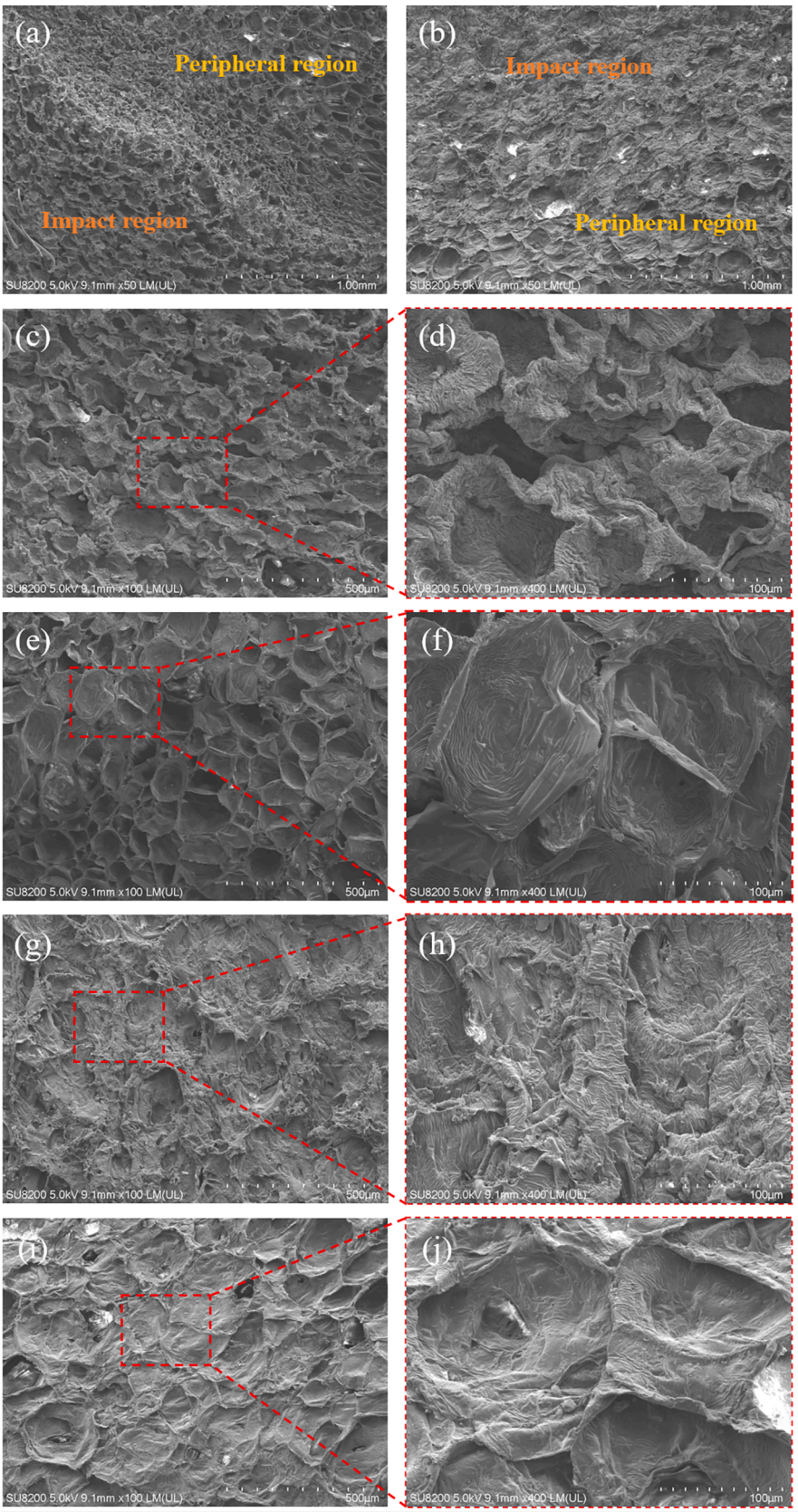

Fig. 15. SEM images of (a) EVA and (b) STG/EVA after ballistic tests; magnified SEM images of EVA in the impact region (c and d) and the peripheral region (e and f); magnified SEM images of STG/EVA in the impact region (g and h) and the peripheral region (i and j).

prominent enhancement was attributed to the outstanding energy absorption capacity and energy transmission property by introducing STG material. In general, the developed STG/EVA foam possessed better mechanical properties and anti-impact performance than plain EVA foam and thus owned promising potential application in personal protective equipment.

Data availability.

The raw/processed data required to reproduce these findings cannot be shared at this time as the data also forms part of an ongoing study.

CRediT authorship contribution statement

Huan Tu: Methodology, Validation, Investigation, Data curation, Writing – original draft. **Pengzhao Xu:** Conceptualization, Formal analysis, Data curation. **Zhe Yang:** Software, Resources. **Fan Tang:** Investigation, Visualization. **Cheng Dong:** Data curation, Validation. **Yuchao Chen:** Investigation, Data curation. **Wenjian Cao:** Methodology, Investigation. **Chenguang Huang:** Conceptualization, Supervision. **Yacong Guo:** Writing – review & editing, Funding acquisition. **Yanpeng Wei:** Writing – review & editing, Supervision, Funding acquisition.

Declaration of Competing Interest

The authors declare that they have no known competing financial interests or personal relationships that could have appeared to influence the work reported in this paper.

Data availability

Data will be made available on request.

Acknowledgements

This work was supported by the National Natural Science Foundation of China (Grant No.12072356 and No.11902329).

References

[1] Brown E, Jaeger HM. Shear thickening in concentrated suspensions: phenomenology, mechanisms and relations to jamming. Rep Prog Phys 2014;77(4).
[2] Brown E, et al. Generality of shear thickening in dense suspensions. Nat Mater 2010;9(3):220–4.
[3] Cheng X, et al. Imaging the microscopic structure of shear thinning and thickening colloidal suspensions. Science 2011;333(6047):1276–9.
[4] Guo F, et al. The static and dynamic mechanical properties of magnetorheological silly putty. Adv Mater Sci Eng 2016;2016:7079698.
[5] Golinelli N, Spaggiari A, Dragoni E. Mechanical behaviour of magnetic Silly Putty: viscoelastic and magnetorheological properties. J Intell Mater Syst Struct 2017;28(8):953–60.
[6] Lu Z, et al. Compressive behaviors of warp-knitted spacer fabrics impregnated with shear thickening fluid. Compos Sci Technol 2013;88:184–9.
[7] Fu K, et al. Low-velocity impact behaviour of a shear thickening fluid (STF) and STF-filled sandwich composite panels. Compos Sci Technol 2018;165:74–83.
[8] Zhang X, et al. Optimization of shear thickening fluid encapsulation technique and dynamic response of encapsulated capsules and polymeric composite. Compos Sci Technol 2019;170:165–73.
[9] Jiang W, et al. Strain rate-induced phase transitions in an impact-hardening polymer composite. Appl Phys Lett 2014;104(12):121915.
[10] Yue X, et al. Multifunctional Janus fibrous hybrid membranes with sandwich structure for on-demand personal thermal management. Nano Energy 2019;63:103808.
[11] Gürgen S, Sert A. Polishing operation of a steel bar in a shear thickening fluid medium. Compos B Eng 2019;175:107127.
[12] Wang Y, et al. Dynamic behavior of magnetically responsive shear-stiffening gel under high strain rate. Compos Sci Technol 2016;127:169–76.
[13] Zhao C, et al. Shear stiffening gels for intelligent anti-impact applications. Cell Rep Phys Sci 2020;1(12):100266.
[14] Tang F, et al. Protective performance and dynamic behavior of composite body armor with shear stiffening gel as buffer material under ballistic impact. Compos Sci Technol 2022;218:109190.
[15] Wang Y, et al. A novel magnetorheological shear-stiffening elastomer with self-healing ability. Compos Sci Technol 2018;168:303–11.
[16] Xu C, et al. Anti-impact response of Kevlar sandwich structure with silly putty core. Compos Sci Technol 2017;153:168–77.
[17] Warren J, et al. Hypervelocity impacts on honeycomb core sandwich panels filled with shear thickening fluid. Int J Impact Eng 2021;150:103803.
[18] Zhang X, et al. Mechanical response of shear thickening fluid filled composite subjected to different strain rates. Int J Mech Sci 2021;196:106304.
[19] Zhao C, et al. Conductive shear thickening gel/Kevlar wearable fabrics: a flexible body armor with mechano-electric coupling ballistic performance. Compos Sci Technol 2019;182:107782.
[20] Myronidis K, et al. Polyborosiloxane-based, dynamic shear stiffening multilayer coating for the protection of composite laminates under Low Velocity Impact. Compos Sci Technol 2022;222:109395.
[21] Asija N, et al. Impact response of Shear Thickening Fluid (STF) treated ultra high molecular weight poly ethylene composites – study of the effect of STF treatment method. Thin-Walled Struct 2018;126:16–25.
[22] Hasanzadeh M, et al. Numerical and experimental investigations into the response of STF-treated fabric composites undergoing ballistic impact. Thin-Walled Struct 2017;119:700–6.
[23] Mishra VD, et al. Ballistic impact performance of UHMWP fabric impregnated with shear thickening fluid nanocomposite. Compos Struct 2022;281:114991.
[24] Tan Z, Li W, Huang W. The effect of graphene on the yarn pull-out force and ballistic performance of Kevlar fabrics impregnated with shear thickening fluids. Smart Mater Struct 2018;27(7):075048.
[25] Yeh SK, et al. Light shear thickening fluid (STF)/Kevlar composites with improved ballistic impact strength. J Polym Res 2019;26(6).
[26] He Q, et al. Impact resistance of shear thickening fluid/Kevlar composite treated with shear-stiffening gel - ScienceDirect. Compos A Appl Sci Manuf 2018;106:82–90.
[27] Gürgen S, Sofuoğlu MA. Integration of shear thickening fluid into cutting tools for improved turning operations. J Manuf Process 2020;56:1146–54.
[28] Gürgen S, Sofuoğlu MA. Smart polymer integrated cork composites for enhanced vibration damping properties. Compos Struct 2021;258:113200.
[29] Sheikhi MR, Gürgen S. Deceleration behavior of multi-layer cork composites intercalated with a non-Newtonian material. Archives of Civil and Mechan Eng 2022;23(1):2.
[30] Gürgen S, et al. Development of eco-friendly shock-absorbing cork composites enhanced by a non-newtonian fluid. Appl Compos Mater 2021;28(1):165–79.
[31] Liu XK, et al. Energy absorption and low-velocity impact response of shear thickening gel reinforced polyurethane foam. Smart Mater Struct 2020;29(4).
[32] Fan T, et al. Multifunctional polyurethane composite foam with outstanding anti-impact capacity for soft body armors. ACS Appl Mater Interfaces 2022;14(11):13778–89.
[33] Prat N, et al. Contemporary body armor: technical data, injuries, and limits. Eur J Trauma Emerg Surg 2012;38(2):95–105.
[34] Messias A, et al. The effectiveness of dental protection and the material arrangement in custom-made mouthguards. Appl Sci 2021;11(20):9363.
[35] Groenewoud WM. Chapter 4 - dynamic mechanical analysis. In: Groenewoud WM, editor. Characterisation of Polymers by Thermal Analysis. Amsterdam: Elsevier Science B.V; 2001. p. 94–122.
[36] Zeltmann SE, et al. Prediction of modulus at various strain rates from dynamic mechanical analysis data for polymer matrix composites. Compos B Eng 2017;120:27–34.
[37] Jose S, et al. Dynamic mechanical properties of immiscible polymer systems with and without compatibilizer. Polym Test 2015;44:168–76.
[38] Poveda RL, Achar S, Gupta N. Viscoelastic properties of carbon nanofiber reinforced multiscale syntactic foam. Compos B Eng 2014;58:208–16.
[39] Zeltmann SE, et al. Prediction of strain rate sensitivity of high density polyethylene using integral transform of dynamic mechanical analysis data. Polymer 2016;101:1–6.
[40] Xianbo, et al. Extracting elastic modulus at different strain rates and temperatures from dynamic mechanical analysis data: a study on nanocomposites. Compos B Eng 2019.
[41] Kostka P, et al. Extension and application of dynamic mechanical analysis for the estimation of spatial distribution of material properties. Polym Test 2016;52:184–91.
[42] Nielsen C, Nemat-Nasser S. Crack healing in cross-ply composites observed by dynamic mechanical analysis. J Mech Phys Solids 2015;76:193–207.
[43] Xie Y-J, et al. Dynamic mechanical properties of cement and asphalt mortar based on SHPB test. Constr Build Mater 2014;70:217–25.
[44] Pham TM, et al. Dynamic compressive properties of lightweight rubberized concrete. Constr Build Mater 2020;238:117705.
[45] Zhang D, et al. Effect of fiber content and fiber length on the dynamic compressive properties of strain-hardening ultra-high performance concrete. Constr Build Mater 2022;328:127024.
[46] Zhou D, et al. Rate-dependent shear banding and fracture behavior in a ductile bulk metallic glass. Mater Sci Eng A 2018;730:270–9.
[47] Fu Q, et al. Impact characterization and modelling of basalt-polypropylene fibre-reinforced concrete containing mineral admixtures. Cem Concr Compos 2018;93:246–59.
[48] Mercy JL, Prakash S. In: *8 - Investigation of damage processes of a microencapsulated self-healing mechanism in glass fiber-reinforced polymers*, in *Modelling of Damage Processes in Biocomposites, Fibre-Reinforced Composites and Hybrid Composites*. Woodhead Publishing; 2019. p. 133–51.
[49] Ansari, I.A. et al., *22 - Fly ash-mixed polymeric media for abrasive flow machining process*, in *Handbook of Fly Ash*, K.K. Kar, Editor. 2022, Butterworth-Heinemann. p. 681-713.